Thermochimica Acta 575 (2014) 238–243

Contents lists available at ScienceDirect

Thermochimica Acta

journal homepage: www.elsevier.com/locate/tca

Crystallization of zirconia doped basalt fibers

Ya.V. Lipatov*, I.V. Arkhangelsky, A.V. Dunaev, S.I. Gutnikov, M.S. Manylov, B.I. Lazoryak

Chemistry Department, Lomonosov Moscow State University, Moscow 119991, Russia

ARTICLE INFO

Article history:
Received 20 September 2013
Received in revised form 31 October 2013
Accepted 4 November 2013
Available online 20 November 2013

Keywords:
Basalt fiber
Zirconia doping
Crystallization mechanism
Non-isothermal kinetics
High temperature stability

ABSTRACT

Crystallization of basalt fibers containing 0–7 wt% ZrO_2 was studied. Fibers were drawn from basalt glasses and annealed in air at different temperatures. Phase composition of obtained samples was determined by XRD. Kinetics of crystallization processes was investigated by DSC. Kinetic models and parameters were estimated for crystallization of spinel-like phase, pyroxene and plagioclase using model-free analysis. It was found that doping of fibers with 1–3 wt% ZrO_2 increased Arrhenius parameters of aluminosilicate crystallization. When the zirconia content was 5–7 wt% the crystallization mechanism significantly changed. This phenomenon resulted in increasing of fiber thermal stability.

1. Introduction

Basalt glasses and fibers possess a number of important properties which make them promising materials in many applications. Due to the high temperature stability (HTS), good mechanical properties and chemical durability they are used as a heat and acoustic insulation [1,2], reinforcing material in composites [3,4] as well as for the production of glass–ceramic materials [5,6]. The main factor determining the HTS of basalt fibers is their crystallization behavior. Crystallization ability primarily depends on fiber chemical composition as well as heat treatment conditions.

The distinctive feature of basalt fiber is a high content of iron oxides ($FeO + Fe_2O_3$ = 8–16 wt%). As a result, crystallization in basalt fiber begins with oxidation of ferrous cations, liquid immiscibility and formation of spinel structure phase on the fiber surface. Oxidation process in air occurs according to the following model: divalent cations (Ca^{2+}, Mg^{2+}, Fe^{2+}) diffuse from the interior of the glass to the surface where they react with environmental oxygen forming nanocrystalline layers CaO, MgO, $(Mg,Fe)_3O_4$. To maintain charge neutrality of the glass, an inward flux of electron holes takes place within the glass [7,8]. With increasing temperature the crystallization of pyroxene phases (mainly augite and diopside) takes place on the spinel crystals which act as nucleation sites [9–11]. Most authors studied crystallization in the bulk glass, while the fibers have a greater degree of homogeneity due to the high cooling rate during manufacturing. At the same time crystallization mechanisms in the bulk glass is similar to those in the fiber. Crystallization of basalt staple fiber was studied in details in papers [1,2,12] where stone wool fibers were used. Papers [13–15] deal with crystallization of continuous basalt fiber during heat treatment. Crystallization ability of basalt fiber can be selectively controlled by doping with other elements.

The addition of zirconium increases glass-transition temperature and thermal stability of sodium borosilicate glass system as well as reduces the rate of phase separation in glass subjected to different heat treatments. Besides, alkali resistance of sodium borosilicate glass [16] and basalt fiber [17] increases. On the other hand, zirconium oxide is known as an agent greatly affecting the nucleation processes in glass–ceramics [18]. The zirconia doping of mullite fiber, obtained by the sol–gel method, can retard the grain growth of mullite during calcination of gel fibers [19].

To the best of our knowledge there are no data on the effect of zirconium oxide on the crystallization and thermal stability of basalt fiber. This paper examines the effect of zirconia addition on the thermal stability, the mechanism and crystallization kinetics of basalt fiber during heat treatment.

2. Experimental

2.1. Sample preparation

Basalt fibers with various zirconia contents were produced in two stages. The first stage included obtaining of zirconia-rich basalt glasses. The glasses were prepared by adding of $ZrSiO_4$ to milled basalt batch. Basalt rock from the Sil'tsevskoe deposit (Carpathians,

* Corresponding author at: Division of Chemical Technology and New Materials, Chemistry Department, Lomonosov Moscow State University, Moscow 119991, Russia. Tel.: +7 905 7723974.
E-mail address: yakov.lipatov@gmail.com (Ya.V. Lipatov).

0040-6031/$ – see front matter © 2013 Elsevier B.V. All rights reserved.
http://dx.doi.org/10.1016/j.tca.2013.11.002

Table 1
EDX analysis of fibers (wt%).

Sample	ZrO_2	Na_2O	MgO	Al_2O_3	SiO_2	K_2O	CaO	TiO_2	Fe_2O_3
Zr0	–	1.9(3)	3.7(4)	15.5(6)	55.6(6)	1.8(2)	8.7(5)	1.0(2)	11.8(6)
Zr1	1.1(2)	1.7(3)	3.5(4)	15.6(6)	55.5(6)	1.7(2)	8.5(5)	1.0(2)	11.4(6)
Zr3	2.8(2)	1.9(3)	3.5(4)	14.9(6)	54.1(6)	1.6(2)	8.5(5)	1.1(2)	11.6(6)
Zr5	5.1(2)	1.9(3)	3.1(4)	14.2(6)	53.8(6)	1.6(2)	8.0(5)	1.0(2)	11.3(6)
Zr7	6.9(2)	2.0(3)	3.0(4)	13.5(6)	53.5(6)	1.3(2)	8.2(5)	1.0(2)	10.6(6)

Ukraine) was used as a raw material. The batch mixture was heated in a platinum crucible in a high-temperature furnace at a rate of 250 °C/h up to 1000 °C and at 30 °C/h in the range of 1000–1600 °C, then homogenized at 1600 °C for 24 h. The molten glass was quenched in water from 1550-1590 °C. It was experimentally found that the solubility limit of zirconia in basalt glass is amounted to 7.0 wt%. Above this threshold, the excess of $ZrSiO_4$ was decomposed into ZrO_2 and SiO_2, which were deposited on the crucible bottom. In this study basalt glasses with zirconia content in the range from 0 to 7 wt% were used. In the second stage basalt fibers were drawn from obtained glasses on a laboratory scale system [15]. The fibers had filament diameters of 10–12 μm. Sizing was not applied in the fiber production. The chemical compositions and specimen designation of fibers are presented in Table 1. Total iron content is expressed as Fe_2O_3. Energy-dispersive X-ray (EDX) analysis was carried out on a JEOL EX-54175 JMH system. Before the examinations all fiber samples were coated with a conducting carbon layer.

2.2. Heat treatment and X-ray diffraction

To identify the crystalline phases and their formation sequence basalt fibers were annealed at 800, 900, 1000 and 1100 °C for 24 h in air. X-ray diffraction (XRD) analysis of annealed fibers was performed at room temperature on a THERMO ARL X'TRA powder diffractometer with a semiconducting Peltier-cooled detector ($CuK_{\alpha 1}$ radiation, $\lambda = 1.54060$ Å, $CuK_{\alpha 2}$ radiation, $\lambda = 1.54443$ Å). XRD patterns were collected in the range of $2\theta = 10°–70°$ with a scan step $2\theta = 0.02°$ and scan rate of 1°/min. Phase analysis was provided using Crystallographica Search-Match software and ICDD PDF-2 database. All fibers before the heat treatment were amorphous.

To determine the content of amorphous phase in samples the grossite $CaAl_4O_7$ as an internal standard was added to the annealed fiber in the ratio of 1:3 (grossite:annealed fiber). The mixture of annealed fiber and grossite was triturated until uniform color was reached. The ratio between internal standard and annealed fiber was chosen so that the intensities of XRD peaks of grossite and crystallized phases were comparable. The following principles were used in choosing internal standard for XRD. Firstly, XRD pattern of standard must have sufficient peaks to determine the content of this phase with high precision. Secondly, peaks of standard must not overlap peaks of annealed basalt fiber. Estimation of the phase content was carried out using Quanto software [20]. The content of amorphous phase G (wt%) was calculated by the following formula (Eq. (1)):

$$G = 100 - \frac{100W_1(100 - W_2)}{W_2(100 - W_1)} \quad (1)$$

where W_1 is the content of added standard (wt%), W_2 is the content of standard obtained by calculation on Quanto (wt%).

2.3. Thermal analysis

Coupled DSC–TG measurements were carried out using NETZSCH STA Jupiter 449 C. The samples of fiber with a mass of 30–40 mg were twisted and placed in a platinum crucible. After that the samples were additionally tamped in a crucible. Measurements were provided at different heating rates 10, 20, 30 K/min in the temperature range of 40–1200 °C in air with a constant flow of 50 ml/min. Temperature and sensitivity of the STA were calibrated against a Netzsch standard kit. Recording of a baseline with empty crucibles was performed for each heating rate. DSC curves were processed using NETZSCH Proteus Analysis software. Glass transition temperature was determined as midpoint temperature according to ASTM E 1356.

NETZSCH Thermokinetics 3.1 software was used to investigate kinetics of the reactions proceeding during fiber heat treatment. Description of principles used in the program can be found in the Opfermann works [21,22]. Detailed procedure for conducting calculation is given in our previous work [23]. At first the Arrhenius parameters of process were estimated by the model-free analysis using Ozawa and Friedman methods [24,25]. The obtained values were used as initial values to solve the direct kinetic problem, i.e. to determine a function characterizing reaction mechanism. This function was found by the nonlinear least-squares method as a function which best approximates (from the statistical viewpoint) the experimental curves for all heating rates used.

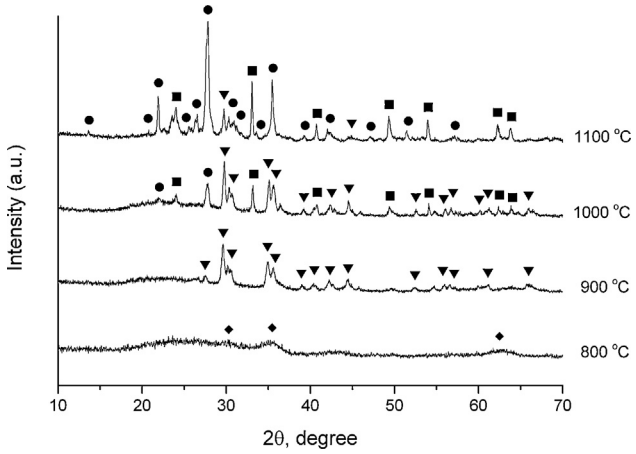

Fig. 1. XRD patterns of Zr0 fiber annealed at 800, 900, 1000 and 1100 °C for 24 h in air (♦ – magnesioferrite, ▼ – pyroxene, ● – plagioclase, ■ – hematite).

3. Results and discussion

3.1. Phase composition of annealed basalt fiber

During the basalt fiber heat treatment, formation of different crystalline phases occurs at different temperatures. The XRD patterns of fiber without ZrO_2 (named Zr0) annealed at various temperatures are shown in Fig. 1. Phase composition of annealed fibers is listed in Table 2. The annealing time at each temperature was 24 h. Data for the samples heated at 20 K/min up to 1200 °C are presented in the DSC columns. It is worth noting that the phase set formed at constant heating rate (DSC mode) is similar to the one obtained at isothermal heat treatment.

The crystallization starts from the formation of spinel structure phase magnesioferrite $MgFe_2O_4$ at 800 °C. At higher temperature magnesioferrite acts as nucleating agent for crystallization

Table 2
Quantitative phase analysis and crystallite size in Zr0 fiber after annealing at 800, 900, 1000, 1100 °C for 24 h and after DSC measurement (dynamic heating at 20 K/min). The relative error in crystallite size calculation equals 3–7%; ±Δ – confidential interval of phase content.

Phase	Phase content, wt%						Crystallite size, nm				
	800 °C	900 °C	1000 °C	1100 °C	DSC	±Δ	800 °C	900 °C	1000 °C	1100 °C	DSC
Amorphous	98	72	52	15	36	2	–	–	–	–	–
Plagioclase	–	–	16	65	48	3	–	–	31	57	34
Pyroxene	–	28	27	11	11	2	–	36	49	46	45
Hematite	–	–	4	9	5	1	–	–	58	71	70
Magnesioferrite	2	–	–	–	–	1	13	–	–	–	–

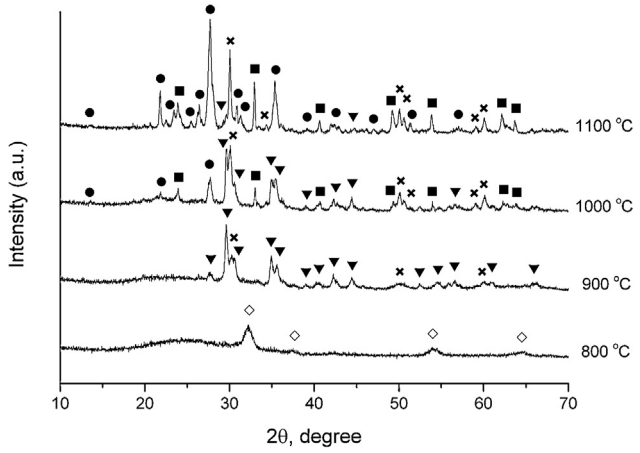

Fig. 2. XRD patterns of Zr5 fiber annealed at 800, 900, 1000 and 1100 °C for 24 h in air (◊ – cubic complex oxide MO_x, where M = Mg, Zr, Ti, × – tetragonal ZrO_2, ▼ – pyroxene, ● – plagioclase, ■ – hematite).

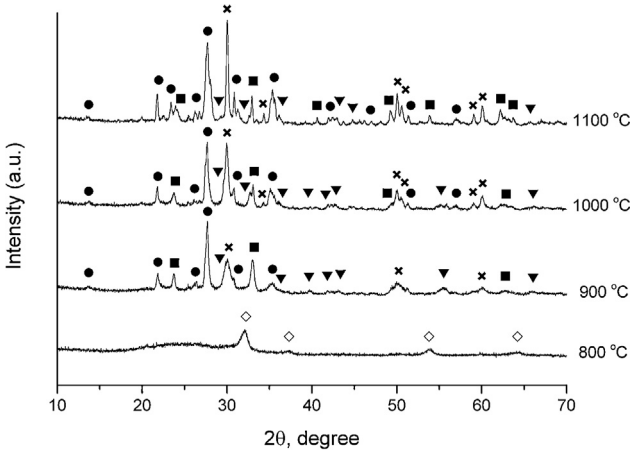

Fig. 3. XRD patterns of Zr7 fiber annealed at 800, 900, 1000 and 1100 °C for 24 h in air (◊ – cubic complex oxide MO_x, where M = Mg, Zr, Ti, × – tetragonal ZrO_2, ▼ – pyroxene, ● – plagioclase, ■ – hematite).

of pyroxenes mainly augite $Ca(Mg,Fe,Al)(Si,Al)_2O_6$ and diopside $CaMgSi_2O_6$. Above 800 °C magnesioferrite is not detected in appreciable quantities. Coherent scattering block size of spinel phase is noticeably less in comparison with pyroxene. It seems that during the pyroxene crystallization iron ions move from the spinel phase to aluminosilicate resulting in decay of magnesioferrite. At temperature above 900 °C hematite α-Fe_2O_3 and plagioclase (solid solution series range from albite $NaAlSi_3O_8$ to anortite $CaAl_2Si_2O_8$ end members) crystallize from amorphous phase. The crystallization mechanisms of fiber with 1–3 wt% ZrO_2 and basalt fiber without ZrO_2 are similar.

When the zirconia content is higher than 5 wt% crystallization sequence changes. At first cubic complex oxide MO_x, where M = Mg, Zr, Ti with a cell parameter a = 4.795(9) Å (NaCl structure type) crystallizes. At the second stage in fiber with 5 wt% ZrO_2 (named Zr5) the formation of pyroxene and tetragonal ZrO_2 occurs. With increasing temperature hematite and plagioclase become the dominant crystalline phases as in the case of basalt fiber without ZrO_2 (Fig. 2). Quantitative phase analysis of Zr5 fiber annealing at various temperatures is shown in Table 3. To calculate the content of MO_x, where M = Mg, Zr, Ti the phase $Mg_{0.33}Zr_{0.33}Ti_{0.33}O_{1.67}$ (ICSD №. 60448) is used as a model structure.

Crystallization mechanism of fiber with maximum ZrO_2 content (named Zr7) is completely different from other samples. After MO_x phase formation simultaneous crystallization of plagioclase, pyroxene, hematite and zirconium oxide takes place at 900 °C (Fig. 3). With increasing temperature up to 1000 °C the pyroxene and plagioclase contents are rising (Table 4). At 1100 °C plagioclase crystallization proceeds, and hematite content slightly increases. Decrease in augite content is caused by its melting. It can be noted that with the increasing of ZrO_2 content its percentage in total crystallinity is rising.

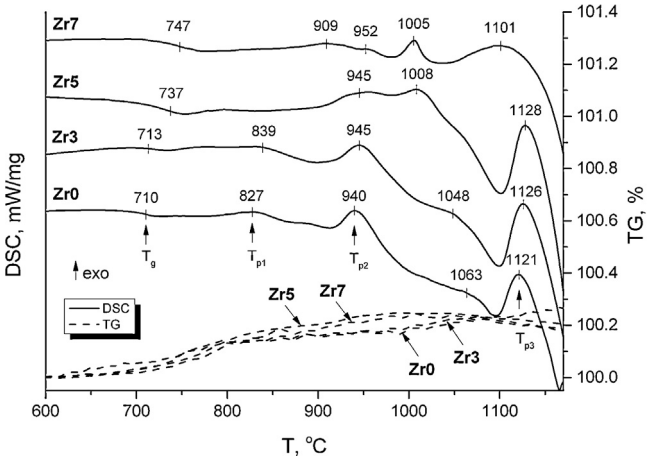

Fig. 4. DSC (solid line) and TG (dash line) curves of fibers with different zirconia contents in air at heating rate of 20 K/min (T_g – glass transition temperature; T_{p1}, T_{p2}, T_{p3} – exothermal peak temperatures).

3.2. Thermal analysis

DSC and TG curves of basalt fiber with different ZrO_2 contents are presented in Fig. 4. The crystallization of basalt fiber without zirconia (named Zr0) occurs in the following way. At first at about 600 °C Fe^{2+} oxidation begins which leads to a slight mass increase (approximately 0.2%). Then at T_g = 710 °C amorphous matrix transits to viscous state resulting in crystallization promotion. Further increase of temperature leads to several exothermal effects on the DSC curve. These effects are caused by the crystallization processes in amorphous phase. In studies [14,15] it was shown that crystallization begins with diffusion of Ca^{2+}, Mg^{2+}, Fe^{2+} ions to the fiber surface and Fe^{2+} oxidation, whereupon the formation

Table 3
Quantitative phase analysis and crystallite size in Zr5 fiber after annealing at 800, 900, 1000, 1100° C for 24 h and after DSC measurement (20 K/min). The relative error in crystallite size calculation equals 3–7%; ±Δ – confidential interval of phase content.

Phase	Phase content, wt%						Crystallite size, nm				
	800 °C	900 °C	1000 °C	1100 °C	DSC	±Δ	800 °C	900 °C	1000 °C	1100 °C	DSC
Amorphous	98	76	58	7	63	2	–	–	–	–	–
Plagioclase	–	–	12	66	26	3	–	–	29	52	31
Pyroxene	–	23	23	16	5	2	–	28	44	31	35
Hematite	–	–	4	7	3	1	–	–	63	71	71
Zirconia	–	1	3	3	3	1	–	16	37	45	45
MO_x	2	–	–	–	–	1	15	–	–	–	–

Table 4
Quantitative phase analysis and crystallite size in Zr7 fiber after annealing at 800, 900, 1000, 1100 °C for 24 h and after DSC measurement (20 K/min). The relative error in crystallite size calculation equals 3–7%; ±Δ – confidential interval of phase content.

Phase	Phase content, wt%						Crystallite size, nm				
	800 °C	900 °C	1000 °C	1100 °C	DSC	±Δ	800 °C	900 °C	1000 °C	1100 °C	DSC
Amorphous	97	55	37	15	56	2	–	–	–	–	–
Plagioclase	–	28	34	58	26	3	–	38	36	36	37
Pyroxene	–	7	20	16	12	2	–	26	45	39	38
Hematite	–	4	4	6	3	1	–	34	40	49	43
Zirconia	–	6	5	5	4	1	–	16	30	47	49
MO_x	3	–	–	–	–	1	14	–	–	–	–

of spinel structure phase occurs [7,8]. In the present paper the effect at T_{p1} = 827 °C refers to the crystallization of spinel-like phase $MgFe_2O_4$ (Fig. 1). According to the XRD data, exothermal effect at T_{p2} = 940°C corresponds to the pyroxene crystallization (mainly augite $Ca(Mg,Fe,Al)(Si,Al)_2O_6$). Pyroxene seems to form on magnesioferrite crystallites, and at the same time iron ions enter into the aluminosilicate composition. At temperature above 1000 °C the viscosity of basalt matrix decreases resulting in fiber conglutination and shrinkage. This phenomenon changes the heat exchange conditions between sample and sensor. It gives rise to quasiendotermal effect in the temperature range of 1080–1100 °C on the DSC curve. Against this background the intensive exothermal effect is observed at T_{p3} = 1121 °C. This effect corresponds to the plagioclase crystallization (Fig. 1, Table 2). The plagioclase crystallization passes into melting of pyroxene and amorphous phase with extremum on the DSC curve at about 1170 °C.

Thus, three clearly defined exothermal effects can be distinguished on the Zr0 DSC curve in the temperature range of 800–1200 °C. Observed effects relate to the successive crystallization of magnesioferrite, pyroxene and plagioclase. It should be pointed out that there is no explicit effect of hematite crystallization at 1000–1100 °C. This may be due to a small content of hematite in total crystallinity and overlapping of its crystallization with quasiendotermal effect.

Zirconia doped fiber during heating behaves as follows. The DSC curves of fibers containing 1–3 wt% ZrO_2 and fiber without zirconia are similar. When the zirconia content is higher than 5 wt% the thermal behavior alters and in the case of 7 wt% changes radically. The first exothermal peak on the Zr5 DSC curve is not distinguishable, and there is a complex effect in the temperature range of pyroxene crystallization which will be discussed in more detail later.

According to XRD data (Table 4), in Zr7 sample pyroxene, plagioclase, hematite and zirconia crystallize simultaneously in the temperature range of 900–1000 °C forming several diffused peaks on the DSC curve. Since the pyroxene content in this temperature range increases greatly it can be concluded that the narrow exoeffect at T_{p2} = 1005 °C corresponds to pyroxene crystallization against the background of other phase crystallization. Crystallization peak of plagioclase is observed at T_{p3} = 1101 °C, further melting of amorphous phase and pyroxene takes place with increasing temperature. Glass transition and exothermal peak temperatures of all fibers are listed in Table 5.

Table 5
DSC data of fibers at heating rate 20 K/min.

Sample	T_g, °C	Exothermal peak temperature		
		T_{p1}, °C	T_{p2}, °C	T_{p3}, °C
Zr0	710 ± 4	827 ± 5	940 ± 6	1121 ± 5
Zr1	712 ± 4	829 ± 5	952 ± 6	1118 ± 5
Zr3	713 ± 4	839 ± 5	945 ± 6	1126 ± 5
Zr5	737 ± 4	–	945 ± 6	1128 ± 5
Zr7	747 ± 4	–	1005 ± 6	1101 ± 5

As follows from the DSC data the glass transition temperature for the Zr5 and Zr7 fibers increases sharply. For the samples with lower zirconia content the glass transition temperature is practically constant. Furthermore, quasiendotermal effect in Zr7 is much less pronounced than in other fibers because of higher viscosity. Consequently, the introduction of more than 5 wt% ZrO_2 in basalt fiber increases HTS.

3.3. Crystallization kinetics

To determine the kinetic parameters of crystallization the experimental DSC curves at three different heating rates (10, 20, 30 K/min) were processed with the Netzsch Thermokinetics software. In solving the direct kinetic problem it was postulated that the all crystallization processes can be presented as one-stage reaction (except for the pyroxene crystallization in Zr5 sample). In the case of basalt fiber without ZrO_2 magnesioferrite crystallization (the first exothermal peak at T_{p1} ~ 830 °C) is well described by the Avrami–Erofeev equation (Eq. (2))

$$f(\alpha) = n(1-\alpha)(-\ln(1-\alpha))^{(n-1)/n} \quad (2)$$

where α is the degree of conversion, n is the dimension of nucleus. Calculated kinetic parameters of crystallization for all samples are presented in Table 6. Crystallization of iron-containing phase (magnesioferrite) occurs due to the Fe^{2+} oxidation. Oxidation proceeds on the fiber surface [1], therefore magnesioferrite nucleation also occurs on the surface with the formation of two-dimensional nucleation since n = 2. The further growth of nuclei takes place along the fiber.

Table 6
Estimated kinetic parameters of crystallization in all fibers.

Sample	Magnesioferrite (T_{p1} ~ 830 °C)			Pyroxene (T_{p2} ~ 950 °C)				Plagioclase (T_{p3} ~ 1120 °C)			
	E_a, kJ/mol	lg A	n	E_a, kJ/mol	lg A	n	a	E_a, kJ/mol	lg A	n	a
Zr0	246 ± 28	10 ± 1	1.9 ± 0.2	196 ± 11	7 ± 1	1.2 ± 0.2	0.60 ± 0.08	841 ± 60	30 ± 3	1.4 ± 0.2	0.50 ± 0.09
Zr1	227 ± 26	9 ± 1	2.0 ± 0.2	308 ± 32	12 ± 1	0.9 ± 0.2	0.50 ± 0.08	862 ± 70	31 ± 3	1.5 ± 0.2	0.50 ± 0.09
Zr3	207 ± 25	8 ± 1	1.8 ± 0.2	311 ± 25	11 ± 1	1.6 ± 0.2	0.55 ± 0.02	1152 ± 100	42 ± 3	2.3 ± 0.3	0.36 ± 0.06
Zr5	–	–	–	241 ± 40	8 ± 1	0.6 ± 0.1	0.43 ± 0.05	1579 ± 60	57 ± 4	2.1 ± 0.2	0.22 ± 0.04
Zr7	–	–	–	277 ± 11	10 ± 1	1.0 ± 0.1	0.7 ± 0.2	–	–	–	–

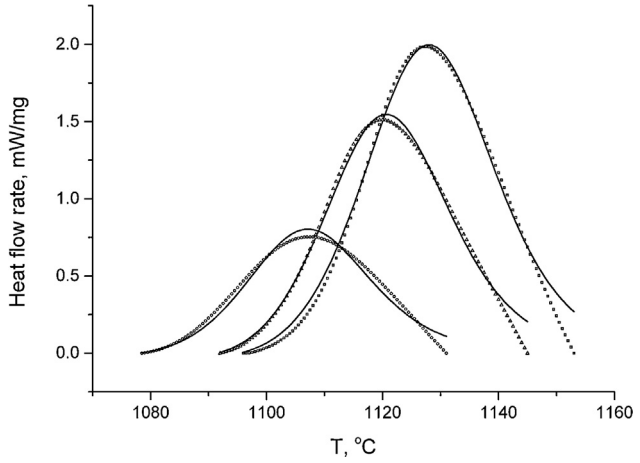

Fig. 5. Graphical comparison of the computation results (solid line) and experimental data (symbols) for DSC curves of plagioclase crystallization in Zr0 basalt fibers. Three heating rates (10, 20, 30 K/min); one-step reaction; the Prout–Tompkins equation.

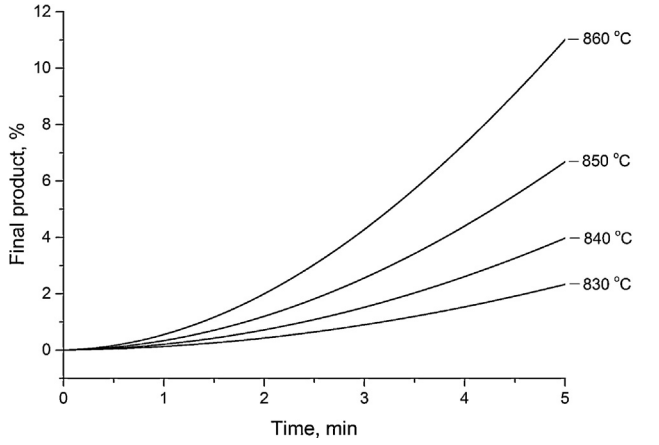

Fig. 6. Isotherms of pyroxene crystallization versus time for Zr0 fiber in air.

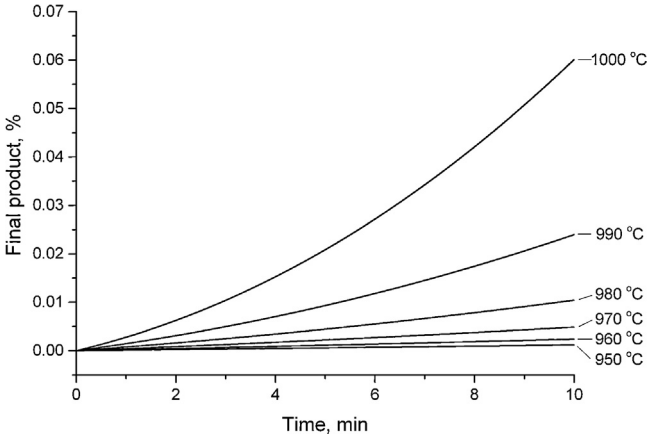

Fig. 7. Isotherms of plagioclase crystallization versus time for Zr0 fiber in air.

Pyroxene crystallization (second exothermal peak at T_{p2} ~ 950 °C) in turn is well approximated by the Prout–Tompkins equation (Eq. (3))

$$f(\alpha) = (1-\alpha)^n \alpha^a \quad (3)$$

where n is reaction order, a is catalysis constant. The Prout–Tompkins equation characterizes the chain branching formation of filamentous nuclei. The applicability of this equation seems logical because pyroxene is chained aluminosilicate.

The third exothermal effect corresponds to plagioclase crystallization. The kinetics of this process, as in the case of pyroxene, is well approximated by the Prout–Tompkins equation (Fig. 5). Plagioclase is aluminosilicate with a framework structure. The activation energy of plagioclase crystallization exceeds the same parameters for pyroxene by several times. It can be assumed that the formation of framework nuclei requires much more energy excess than linear nuclei.

One of the important aspects in crystallization mechanism is to determine initiator in the pyroxene nucleation. For this purpose it is necessary to calculate the pyroxene content, which could be formed under isothermal conditions in the temperature range of magnesioferrite crystallization using kinetic data (Table 6). The degree of pyroxene crystallization versus time at different temperatures is shown in Fig. 6. As follows from the presented data, the pyroxene may crystallize in this temperature range. Therefore the crystallization is most probably initiated by magnesioferrite crystallites. In addition pyroxene has the iron ions in its composition. It seems that magnesioferrite decomposes at pyroxene crystallization temperatures because of the transition of iron ions from spinel-like phase to pyroxene. The XRD studies have not detected $MgFe_2O_4$ in samples annealed at temperature above 900 °C. Successive crystallization of magnesioferrite and pyroxene appears in a decrease of activation energy for the pyroxene crystallization as well (Table 6).

To determine the pyroxene role in plagioclase crystallization it is necessary to apply a method previously used. The degree of plagioclase crystallization versus time at different temperatures is presented in Fig. 7. These temperatures enter into the pyroxene crystallization range. According to the isotherms, plagioclase does not crystallize in the temperature range of pyroxene formation to any significant extent. At this temperature the viscosity of amorphous phase is reduced, and the fiber loses its original morphology due to fiber conglutination and spreads as a liquid mass. As follows from XRD data collected on a sample annealed at 1000 °C the hematite crystallization occurs and the liquid–solid interface appears. It can be assumed that plagioclase nuclei are formed on this interface.

The addition of a small amount of ZrO_2 (1–3 wt%) to the fiber does not change the crystallization mechanism. At the same time, the Arrhenius parameters for crystallization of pyroxene and

plagioclase increase in these samples (Table 6). The function of the reaction rate is also described by the Prout–Tompkins. This behavior seems to be caused by increase in viscosity of the amorphous matrix by zirconia addition that hinders the formation of chain and framework aluminosilicates.

The first phase in Zr5–Zr7 crystallization becomes the complex oxide MO_x, where M = Mg, Zr, Ti. The crystallization peak of this phase is poorly resolved on the DSC curve and is not suitable for the formal kinetic analysis. For this reason, the crystallization kinetic parameters of the first phase are presented only for Zr0–Zr3 samples.

On the DSC curve of Zr5 fiber the second and the third exoeffects are observed at the same temperatures as in the previous samples despite an increase of glass transition temperature (Table 5). However, there is a complex effect in pyroxene crystallization range (Fig. 4). Calculations have shown that this effect is well approximated by a two-stage scheme of parallel processes (Eq. (4)):

$$\begin{array}{l} \nearrow \mathrm{B} \\ \mathrm{A} \\ \searrow \mathrm{C} \end{array} \qquad (4)$$

The first process A→B is characterized by the Prout–Tompkins equation with kinetic parameters which are typical to the pyroxene crystallization from amorphous phase. The Arrhenius parameters of this process are listed in Table 6. The second process A→C is described by the Avrami–Erofeev equation with the following kinetic parameters: $E_a = 2650 \pm 210$ kJ/mol, $\lg A = 108 \pm 8$ and $n = 0.8 \pm 0.1$. This process can be attributed to the zirconia crystallization that is confirmed by the XRD data (Fig. 2, Table 3). The Arrhenius parameters of the plagioclase crystallization at $T_{p3} = 1128\,^{\circ}C$ are significantly higher than for the previous samples. Thus, at the zirconia content higher than 5 wt% the crystallization mechanism of basalt fiber changes.

There are several diffused exoeffects on the DSC curve of Zr7 sample. Only one narrow symmetric peak is observed at 1005 °C (Fig. 4). As follows from the calculation, the peak is well approximated by the Prout–Tompkins equation with parameters specific to the pyroxene crystallization (Table 6). Since several phases crystallize in this temperature range, it can be assumed that the pyroxene formation is a rate-limiting step.

4. Conclusions

It is shown that DSC and XRD enable us to identify processes occurring in basalt fiber under heat treatment. The glass transition is followed by formation of spinel-like phase. In its turn the pyroxene crystallization is initiated by formation of spinel-like phase. Further temperature increase leads to the simultaneous plagioclase crystallization and melting of amorphous phase and pyroxene.

It is found that zirconia doping of basalt fiber significantly changes the mechanism and kinetics of crystallization. A small amount of zirconia increases the Arrhenius parameters of pyroxene and plagioclase crystallization. Nevertheless, the crystallization mechanism remains the same as in the case of fibers without zirconia.

More than 5 wt% of ZrO_2 modifies the crystallization behavior. The first phase appeared under heat treatment is cubic complex oxide MO_x, where M = Mg, Zr, Ti with a cell parameter $a = 4.795(9)$ Å. The nuclei of this phase become the crystallization centers for pyroxene and zirconium oxide. For the fibers containing less than 5 wt% ZrO_2 all crystallization processes are one-stage reactions. Further increase of ZrO_2 content leads to simultaneous crystallization of pyroxene and zirconia according to a two-stage scheme of parallel reactions with different mechanisms. Simultaneous crystallization of plagioclase, pyroxene, hematite and zirconia takes place in basalt fiber with 7 wt% ZrO_2.

When the zirconia content is higher than 5 wt% the glass transition temperature considerably increases resulting in growth of HTS. However, maximum ZrO_2 content in basalt fiber does not exceed 7 wt%.

Thus, doping of basalt fibers with zirconia significantly effects on crystallization of aluminosilicate phases. Modification of crystallization mechanism is reflected in the change of phase composition and kinetic parameters as well as in the glass transition and crystallization peak temperatures.

Acknowledgment

The authors express gratitude to Dr. Valery Efremov for his help in the discussion of XRD data and for valuable advices.

References

[1] M.M. Smedskjaer, M. Solvang, Y. Yue, Crystallisation behaviour and high-temperature stability of stone wool fibres, J. Eur. Ceram. Soc. 30 (2010) 1287–1295.
[2] M. Moesgaard, H.D. Pedersen, Y.Z. Yue, E.R. Nielsen, Crystallization in stone wool fibres, J. Non-Cryst. Solids 353 (2007) 1101–1108.
[3] V. Lopresto, C. Leone, I. De Iorio, Mechanical characterisation of basalt fibre reinforced plastic, Composites Part B 42 (2011) 717–723.
[4] J. Sim, C. Park, D.Y. Moon, Characteristics of basalt fiber as a strengthening material for concrete structures, Composites Part B 36 (2005) 504–512.
[5] A. Karamanov, P. Pisciella, C. Cantalini, M. Pelino, Influence of Fe^{3+}/Fe^{2+} ratio on the crystallization of iron-rich glasses made with industrial wastes, J. Am. Ceram. Soc. 83 (2000) 3153–3157.
[6] A. Karamanov, G. Taglieri, M. Pelino, Sintering behavior and properties of iron-rich glass–ceramics, J. Am. Ceram. Soc. 87 (2004) 1571–1574.
[7] R.F. Cooper, J.B. Fanselow, D.B. Poker, The mechanism of oxidation of a basaltic glass: chemical diffusion of network-modifying cations, Geochim. Cosmochim. Acta 60 (1996) 3253–3265.
[8] G.B. Cook, R.F. Cooper, T. Wu, Chemical diffusion and crystalline nucleation during oxidation of ferrous iron-bearing magnesium aluminosilicate glass, J. Non-Cryst. Solids 120 (1990) 207–222.
[9] A. Karamanov, S. Ergul, M. Akyildiz, M. Pelino, Sinter-crystallization of a glass obtained from basaltic tuffs, J. Non-Cryst. Solids 354 (2008) 290–295.
[10] A. Karamanov, M. Pelino, Crystallization phenomena in iron-rich glasses, J. Non-Cryst. Solids 281 (2001) 139–151.
[11] A. Karamanov, P. Pisciella, M. Pelino, The crystallisation kinetics of iron rich glass in different atmospheres, J. Eur. Ceram. Soc. 20 (2000) 2233–2237.
[12] Y. Yue, M. Korsgaard, L.F. Kirkegaard, G. Heide, Formation of a nanocrystalline layer on the surface of stone wool fibers, J. Am. Ceram. Soc. 92 (2009) 62–67.
[13] E.A. Moiseev, S.I. Gutnikov, A.P. Malakho, B.I. Lazoryak, Effect of iron oxides on the fabrication and properties of continuous glass fibers, Inorg. Mater. 44 (2008) 1026–1030.
[14] M.S. Manylov, S.I. Gutnikov, Ya.V. Lipatov, K.V. Pokholok, D.S. Filimonov, B.I. Lazoryak, Kristallizacija bazal'tovyh nepreryvnyh volokon v okislitel'noj atmosfere, Fizika i Himija Stekla 38 (2012) 565–573 (in Russian).
[15] S.I. Gutnikov, M.S. Manylov, Ya.V. Lipatov, B.I. Lazoryak, K.V. Pokholok, Effect of the reduction treatment on the basalt continuous fiber crystallization properties, J. Non-Cryst. Solids 368 (2013) 45–50.
[16] M. Hasanuzzaman, M. Sajjia, A. Rafferty, A.G. Olabi, Thermal behaviour of zircon/zirconia-added chemically durable borosilicate porous glass, Thermochim. Acta 555 (2013) 81–88.
[17] Ya.V. Lipatov, S.I. Gutnikov, M.S. Manylov, B.I. Lazoryak, Effect of ZrO_2 on the alkali resistance and mechanical properties of basalt fibers, Inorg. Mater. 48 (2012) 751–756.
[18] S. Banijamali, B. Eftekhari Yekta, H.R. Rezaie, V.K. Marghussian, Crystallization and sintering characteristics of $CaO–Al_2O_3–SiO_2$ glasses in the presence of TiO_2, CaF_2 and ZrO_2, Thermochim. Acta 488 (2009) 60–65.
[19] W. Wang, D. Weng, X. Wu, Preparation and thermal stability of zirconia-doped mullite fibers via sol–gel method, Progr. Nat. Sci.: Mater. Int. 21 (2011) 117–121.
[20] A. Altomare, M.C. Burla, C. Giacovazzo, A. Guagliardi, A.G.G. Moliterni, G. Polidori, et al., Quanto: a Rietveld program for quantitative phase analysis of polycrystalline mixtures, J. Appl. Crystallogr. 34 (2001) 392–397.
[21] J. Opfermann, Kinetic analysis using multivariate non-linear regression. I. Basic concepts, J. Therm. Anal. Calorim. 60 (2000) 641–658.
[22] J.R. Opfermann, E. Kaisersberger, H.J. Flammersheim, Model-free analysis of thermoanalytical data-advantages and limitations, Thermochim. Acta 391 (2002) 119–127.
[23] I.V. Arkhangel'skii, A.V. Dunaev, I.V. Makarenko, N.A. Tikhonov, S.S. Belyaev, A.V. Tarasov, Non-isothermal Kinetic Methods, Edition Open Access, Max Planck Research Library, Berlin, 2013.
[24] T. Ozawa, A new method of analyzing thermogravimetric data, Bull. Chem. Soc. Jpn. 38 (1965) 1881–1886.
[25] H.L. Friedman, Kinetics of thermal degradation of char-forming plastics from thermogravimetry. Application to a phenolic plastic, J. Polym. Sci. Part C: Polym. Symp. 6 (1964) 183–195.